

# Effect of hollow sphere size and size distribution on the quasi-static and high strain rate compressive properties of Al-A380–Al<sub>2</sub>O<sub>3</sub> syntactic foams

Joseph A. Santa Maria · Benjamin F. Schultz ·  
J. B. Ferguson · Nikhil Gupta · Pradeep K. Rohatgi

Received: 13 August 2013 / Accepted: 7 October 2013 / Published online: 19 October 2013  
© Springer Science+Business Media New York 2013

**Abstract** Metal matrix syntactic foams are promising materials for energy absorption; however, few studies have examined the effects of hollow sphere dimensions and foam microstructure on the quasi-static and high strain rate properties of the resulting foam. Aluminum alloy A380 syntactic foams containing Al<sub>2</sub>O<sub>3</sub> hollow spheres sorted by size and size range were synthesized by a sub-atmospheric pressure infiltration technique. The resulting samples were tested in compression at strain rates ranging from 10<sup>-3</sup> s<sup>-1</sup> using a conventional load frame to 1720 s<sup>-1</sup> using a Split Hopkinson Pressure-bar test apparatus. It is shown that the quasi-static compressive stress–strain curves exhibit distinct deformation events corresponding to initial failure of the foam at the critical resolved shear stress and subsequent failures and densification events until the foam is deformed to full density. The peak strength, plateau strength, and toughness of the foam increases with increasing hollow

sphere wall thickness to diameter ( $t/D$ ) ratio. Since  $t/D$  was found to increase with decreasing hollow sphere diameter, the foams produced with smaller spheres showed improved performance. The compressive properties did not show measurable strain rate dependence.

## Introduction

Metallic foams are a broad class of porous materials that contain either open or closed cell type porosity and compared to fully dense metals, exhibit lower density, and higher specific properties including stiffness, energy absorption, surface area, and mechanical and acoustical damping capacities [1–6]. Some of the metal foams are commercially produced and have found use as cores in sandwich composite panels, filters, heat exchangers, flotation devices, energy absorbers and as decorative building materials. A class of foam material, where the voids are contained within hollow spheres that are embedded in a metallic matrix, termed metal matrix syntactic foams (MMSFs), offers opportunities to tailor the properties of these energy absorbing materials. MMSFs have been synthesized by pressure infiltration, stir casting, and powder metallurgy methods with a variety of matrices including aluminum [7–27], magnesium [28, 29], zinc [30], iron [15, 27, 31, 32], and titanium [15, 33] alloys. Various hollow spheres have been used including fly ash [7, 10–12, 15–22, 26, 30, 33], mullite [8, 9], Al<sub>2</sub>O<sub>3</sub> [23–25, 32], low carbon steel [27, 31], stainless steel [27, 31], and carbon [28].

The compressive stress–strain curves of metal foams exhibit an initial elastic region up to a plateau stress, which is maintained until a relatively large strain is reached. At this point the material again begins to deform with a large increase in stress for a given strain (densification). MMSFs

---

J. A. Santa Maria · B. F. Schultz (✉) · J. B. Ferguson ·  
P. K. Rohatgi  
Materials Science and Engineering Department, University  
of Wisconsin-Milwaukee, 3200 N Cramer St., Milwaukee,  
WI 53201, USA  
e-mail: bfs2@uwm.edu

J. A. Santa Maria  
e-mail: jas25@uwm.edu

J. B. Ferguson  
e-mail: jbf2@uwm.edu

P. K. Rohatgi  
e-mail: prohatgi@uwm.edu

N. Gupta  
Mechanical and Aerospace Engineering Department,  
Polytechnic Institute of New York University, 6 MetroTech  
Center, Brooklyn, NY 11201, USA  
e-mail: ngupta@poly.edu

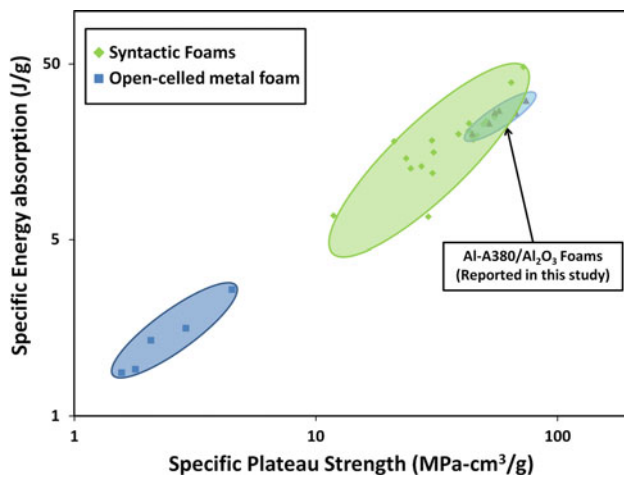


**Fig. 1** Log–log plot of specific plateau strength and specific energy absorption for different types of foams. Ovals enclose syntactic foams and open-cell foams, respectively [4–6, 8–13, 16, 27, 30, 31]

differ slightly from the typical behavior of foams, in that the initial elastic region ends in a peak stress, after which the stress drops and then gradually increases until densification. The properties of MMSFs are, therefore, most often characterized by the peak stress, plateau stress, densification strain, and energy absorption until densification. An Ashby style log–log chart showing the specific plateau strength versus the specific energy absorption for a variety of open-celled and syntactic foams is shown in Fig. 1. Although different studies use differing definitions of densification strain, the definition for the purposes of Fig. 1 is the past-peak strain at which the stress returns to the initial peak stress. This figure shows the potential superiority of MMSFs over open-cell foams in terms of both specific plateau strength and specific energy absorption capacity. The objective of many of the studies involving syntactic foams is to increase both the specific energy absorption and specific plateau strength. Further enhancement in the energy absorption characteristics will be facilitated by a greater understanding of the effects of processing, microstructure design and composition on the quasi-static, and dynamic properties of these materials. The following paragraphs outline some of the key findings that can be used in the design of syntactic foams.

Balch and Dunand [9] used in situ synchrotron and neutron diffraction techniques to measure elastic strains in commercially pure (c.p.) Al and Al-7075/mullite hollow microsphere (15–75  $\mu\text{m}$  diameter) reinforced syntactic foams in an attempt to quantify their deformation behavior and to identify the degree of load transfer that occurs between the microspheres and the foam matrix during compression. In each case, the matrix exhibited elastic behavior up to yielding after which the load is transferred to the spheres that continue to deform

elastically. The 7075 alloy reacted with the mullite spheres resulting in the transformation of the spheres to aluminum oxide and the release of Si in the form of particles into the surrounding matrix. These Si particles acted as reinforcements to the matrix, unloading the spheres, and decreasing their overall contribution to the deformation of the syntactic foam. Though the strains applied in this study did not result in fracture of the microspheres, it is clearly evident that the matrix composition and the properties of the hollow sphere both factor into the peak strength of the syntactic foam.

Zhang et al. [12] examined the deformation behavior of c.p. aluminum/fly ash (124  $\mu\text{m}$  average diameter) syntactic foams under quasi-static compression conditions until strains of 55 % were reached and the material had begun to densify. Micro-CT measurements were then used to characterize the deformation of the foam. As the strain increased beyond the linear elastic region fly ash cenospheres appeared to collapse in random locations in the sample, followed by more general collapse of spheres in bands and densification via localized plasticity. The seemingly random crushing of spheres was attributed to the dispersion and size range of the spheres, where larger spheres would crush first followed by smaller spheres, though little information was given on the size characteristics of the hollow microspheres. Tao et al. [13] reported similar phenomenon in the case where bimodal size distributions of ceramic ( $\sim 60\%$   $\text{SiO}_2$ -  $\sim 40\%$   $\text{Al}_2\text{O}_3$  and 0.4–0.5 %  $\text{Fe}_2\text{O}_3$ ) microspheres were incorporated in 6082-Al. The greatest strength and energy absorption was obtained with a uniform composition of fine microspheres (75–125  $\mu\text{m}$  diameter). As an increasing amount of coarser (250–500  $\mu\text{m}$  diameter) microspheres was added up to 70 vol%, the peak and plateau strengths and energy absorption of the foams decreased due to the failure of the coarser particles and resulting localized strain. This demonstrates the importance of the size range and distribution of the spheres on the resulting properties of the syntactic foam.

Kiser et al. [23] showed that the peak stress of A201 (O and T6 conditions) and A360-O reinforced with  $\text{Al}_2\text{O}_3$  hollow spheres (1, 1.5, and 2.5 mm diameter) markedly increases with increasing ratio of the hollow sphere wall thickness to the diameter ( $t/D$ ) ratio of the spheres. Deformation occurred by local crushing of spheres in either  $45^\circ$  angle bands in relation to the loading direction or normal to the loading direction which was attributed to strain localization. Unconstrained compression tests were suspended after approximately 7–15 % strain was achieved as the localized failures resulted in large sections of the specimens breaking off. As a consequence, the dependence of the energy absorption of the syntactic foam until densification could not be determined.

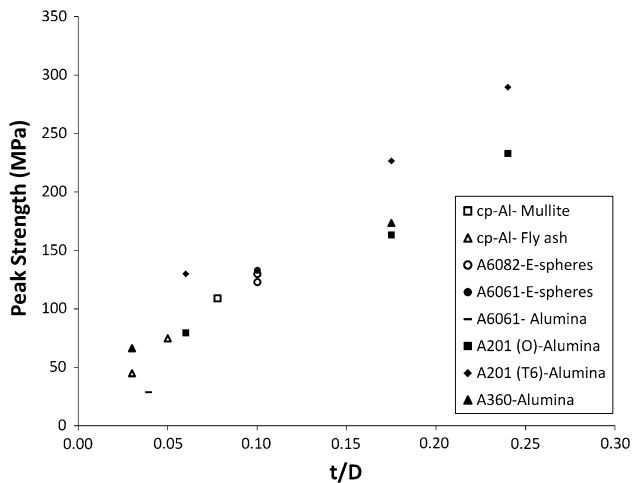


**Fig. 2** Effect of  $t/D$  ratio on the peak strength of various Aluminum alloy-hollow sphere metal matrix syntactic foams [8, 10, 11, 15, 23, 24, 26]

There is a relative absence of systematic studies on the effect of sphere diameter,  $t/D$  ratio, and size range on the quasi-static properties of MMSFs; however, review of the published quasi-static compressive properties shows that the peak strength generally increases with increasing  $t/D$  ratio as shown in Fig. 2. In addition to the  $t/D$  ratio, the size range of the hollow spheres in the syntactic foam will also likely affect the packing efficiency and resulting volume percentage of spheres in the composite. The objective of this study is to elucidate the effect of size of the hollow spheres, size range and  $t/D$  ratio on the quasi-static, and high strain rate compressive properties of aluminum alloy matrix syntactic foams.

**Experimental procedure**

Syntactic foams composed of aluminum alloy A380 reinforced with approximately 40–50 vol% hollow  $Al_2O_3$  hollow spheres (ALODUR white bubble alumina) were synthesized. The nominal compositions of the alloy and the hollow spheres are presented in Table 1 (information provided by suppliers). The hollow spheres were supplied by C–E Minerals in standard size (diameter) ranges of 0–0.5, 1–3, and 1–5 mm. The spheres were further sorted by size using an Allen Bradley Sonic Sifter to produce 6 size ranges for comparison. After sorting, the  $Al_2O_3$  spheres were floated in chloroform ( $CHCl_3$ ) which has a density of  $1.483\text{ g/cm}^3$ , causing the defective spheres to sink and the intact spheres to float allowing them to be collected. The bulk density of the hollow spheres for each size range was determined by measuring the mass of a fixed amount of spheres and the corresponding volume of water displaced by these same spheres. The size ranges evaluated in this

**Table 1** Nominal composition of matrix and reinforcements

Material	Component	Nominal content (wt%)
A380	Al	85.5–89.5
	Si	7.5–9.5
	Cu	3–4
	Fe	0.6
	Mg	0.1
	Ni	0.1
	Zn	0.1
	$Al_2O_3$ hollow sphere	$Al_2O_3$
	$SiO_2$	0.8
	$Na_2O$	0.1
	MgO	0.05
	$Fe_2O_3$	0.03
	CaO	0.03

study along with their measured densities are shown in Table 2.

The method of sub-atmospheric pressure infiltration used for MMSF synthesis is described in detail elsewhere [21] and is summarized below. A 13.95 mm ID borosilicate test tube was tap-packed with hollow spheres to a height of 70–90 mm. An ingot of aluminum alloy was placed above the hollow spheres, separated by a 2-mm-thick layer of zirconia felt. The felt was used as a reaction barrier between the aluminum alloy melt and the spheres prior to infiltration and served as a filter to remove the oxide layer from the liquid melt. The crucible containing the preform and ingot was heated in a quartz chamber under vacuum to  $750\text{ }^\circ\text{C}$  and held for 20 min at which time the alloy had fully melted and uniformly sealed the inner circumference of the crucible. Argon gas was then rapidly introduced into the heated quartz chamber, reaching a sub-atmospheric pressure of 0.4 bar within 10 s, thereby forcing the molten alloy into the evacuated spaces between the hollow spheres. The quartz chamber containing the sample was then removed from the tube furnace and the sample was allowed to cool in air under sub-atmospheric pressure of 0.4 bar for 3 min by which time the sample had solidified. The sample was then removed and quenched in room-temperature water. Specimens of the unreinforced alloy were cast using the same procedure for comparison. The density of the composites was measured using a Metler Toledo AT261 Delta Range Microbalance equipped with a density measurement apparatus (Archimedes method). The specimens were first lightly coated with vacuum grease to prevent infiltration of surface pores during the density measurement. Microstructural analysis was performed with a Nikon Eclipse TS100 microscope equipped with an automated stage and Clemex Professional Image analysis software, and a Hitachi S4800 FE-SEM equipped with a Bruker Quantax EDS System.

**Table 2** Average composite density and A% matrix

Sieve size range (mm)	Hollow sphere bulk density (g/cc)	Composite density (g/cc)	Area % matrix	Average size of infiltrated spheres (mm)	% filled spheres in foam specimen
0.212–0.425	1.33	1.86	35.7–46	0.314	2.07
0.425–0.85	1.24	1.89	37.9–44.2	0.544	2.53
0.85–1	1.12	1.9	38.3–51.4	0.860	4.11
0–0.5	1.28	1.86	42.5–51.9	0.370	0.08
1–2	0.97	1.98	41.4–51.9	0.936	5.00
0–2	1.28	1.90	41.3–65.5	1.217	19.77

Quasi-static compression testing was performed in accordance with ASTM C365-94 on cylindrical specimens (diameter = 14.3 mm and length = 12.7 mm). Testing was carried out using a SATEC Model 50Ud Universal Testing Machine at constant crosshead speed with an initial strain rate of  $10^{-3} \text{ s}^{-1}$  and a self-leveling platen. Strains were calculated from the crosshead displacement, and were corrected for deflection of the load frame. A minimum of 6 specimens were tested for each syntactic foam composition. The quasi-static compression curves typically exhibited an initial peak followed by a lower plateau stress and later densification. Compression was stopped at the densification strain, defined as the strain following the initial peak strength at which the stress reaches the magnitude of the initial peak stress (approximately 45 % strain). For comparison to other studies concerning Al alloy- $\text{Al}_2\text{O}_3$  syntactic foams, selected specimens were tested to 60 % strain. The plateau strength reported is the average measured strength from initial peak to densification. The toughness of the MMSFs was determined by calculating the area under the quasistatic compressive stress–strain curve up to the densification strain and has units corresponding to the energy per unit volume of the material ( $\text{J}/\text{cm}^3$ ). Optical and SEM microscopy was carried out on polished cross sections of the quasi-statically tested specimens.

A Split Hopkinson bar test apparatus was used to obtain high strain rate compressive properties of syntactic foams produced with 0.425–0.85 mm OD and 0.85–1 mm OD hollow spheres. Details of the test apparatus and methods are discussed at length elsewhere [35, 36] and are summarized as follows. Cylindrical specimens of the two foams were prepared with 10 mm diameter and 5 mm thickness. The specimens were nested between Inconel incident and transmitter bars having Young's modulus, density, and sound wave velocity of 195 GPa,  $8190 \text{ kg}/\text{m}^3$ , and 4802 m/s, respectively. Once a test is performed by launching a striker bar into the incident bar which crushes the specimen, data from strain gages mounted in the centers of the incident and transmitter bar, along with the bar and specimen dimensions are used to back-calculate the strain rate. In this work, strain rates between 880 and  $1720 \text{ s}^{-1}$  were achieved. Although adiabatic

heating during high strain rate testing of aluminum can significantly affect the measured flow stress, testing was performed only to relatively low strains where corrections tend to be small and thus can be neglected [37, 38].

## Results and discussion

### Microstructure

The properties of the matrix depend on the fineness of the microstructure and the distribution of phases that form as a result of the solidification sequence and inter-relationships between the large number of alloying elements in A380 alloy. Several studies have been published on the solidification sequence of this alloy at different cooling rates and containing different variations of Cu, Fe, Mg, Mn, Zn, Ti, Ni, and Cr [39–41]. The solidification sequence that is observed for this alloy can be summarized as follows:

- 1) Formation of  $\alpha$ -Aluminum dendrites
- 2) Precipitation of Al–Mn–Fe precipitates including  $\text{Al}_{15}(\text{Mn},\text{Fe})_3\text{Si}_2$  and the  $\text{Al}_5\text{FeSi}$  needles.

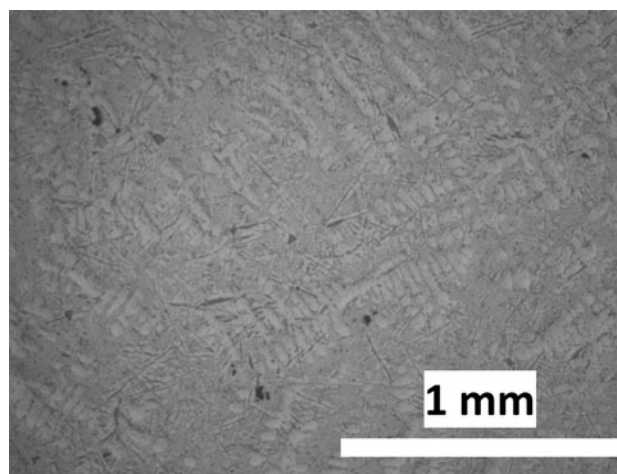


**Fig. 3** Microstructure of the base alloy A380 cast under similar conditions ( $\times 50$ ). Dendritic networks of primary Al, primary Si, possible  $\text{Al}_{15}(\text{Fe},\text{Mn})_3\text{Si}_2$ , and porosity are observed

- 3) Eutectic reaction of Si and Mn, Fe containing phases
- 4) Precipitation of  $Mg_2Si$ , apparent as black particles (this is only likely if the Mg content is high)
- 5) Precipitation of  $Al_2Cu$
- 6) Formation of complex eutectics containing  $Al_2Cu$  and  $Al_5Mg_8SiCu_2$

The microstructure of the matrix cast under the same conditions as the syntactic foams is shown in Fig. 3. Networks of primary aluminum are clearly visible, along with primary Si, needle-like precipitates likely to be  $Al_3FeSi$  and finer phases that are likely combinations of  $Al_{15}(Fe, Mn)_3Si_2$ , complex eutectics, and  $Al_2Cu$ .

In the case of a composite, the matrix alloy composition can vary due to reaction with the reinforcement, which will

alter the phases that form upon solidification. Magnesium present in the syntactic foam for example is likely to react with the  $Al_2O_3$  hollow spheres to form  $MgAl_2O_4$ ; however, this is not likely to influence the solidification structure significantly, as it was found by Gowri and Samuel [41] that the solidification of an alloy containing three times the standard amount of Mg resulted only in a coarsening of the  $Al_{15}(Mn, Fe)_3Si_2$  phase and did not result in the formation of observable amounts of  $Mg_2Si$ .

Representative micrographs of the as-cast composites are shown in Fig. 4. The hollow spheres appear to be uniformly distributed, and fully encapsulated by the metal matrix with little to no visible interstitial porosity. The  $t/D$  ratio may be determined by considering the sphere

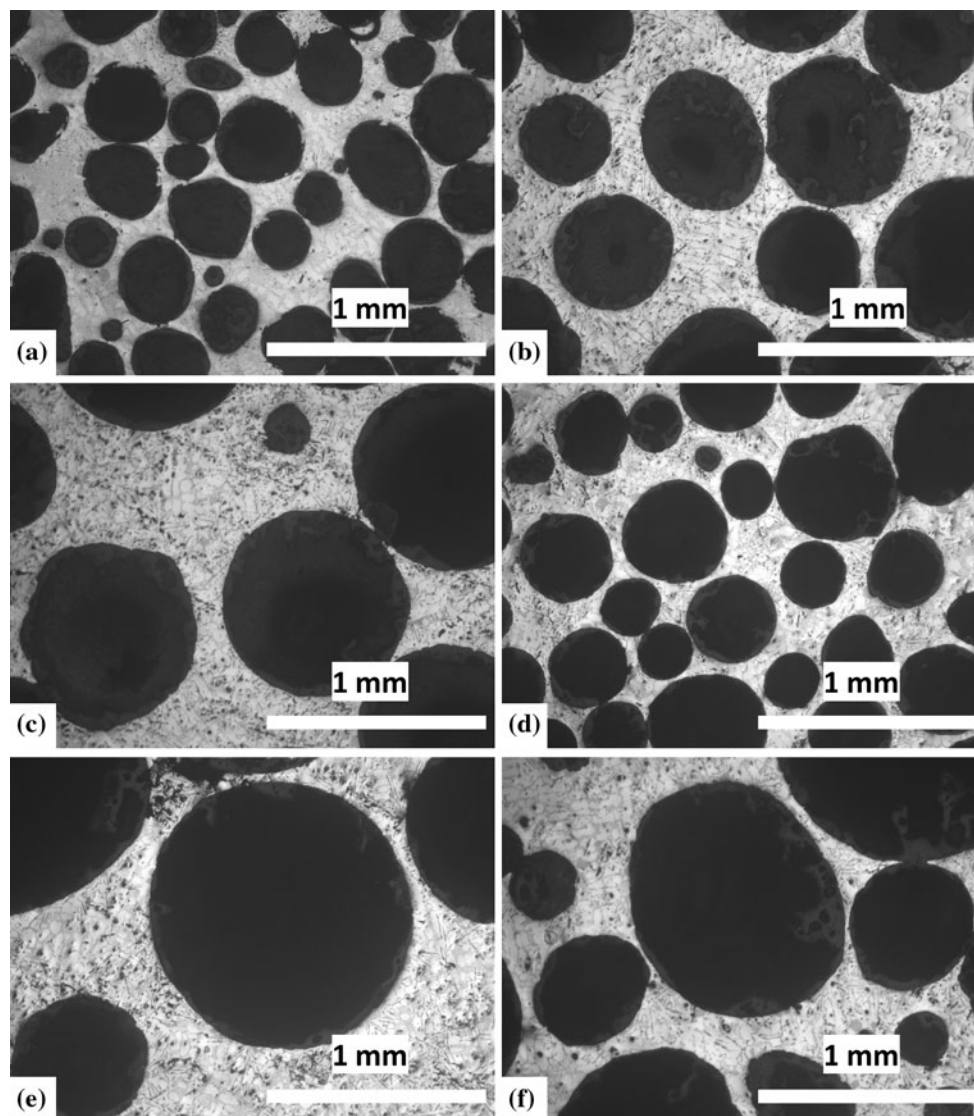


**Fig. 4** Representative microstructures of A380– $Al_2O_3$  syntactic foams containing hollow spheres with diameters **a** 0.212–0.425 mm, **b** .425–0.85 mm, **c** 0.85–1 mm, **d** 0–0.5 mm, **e** 1–2 mm, and **f** 0–2 mm

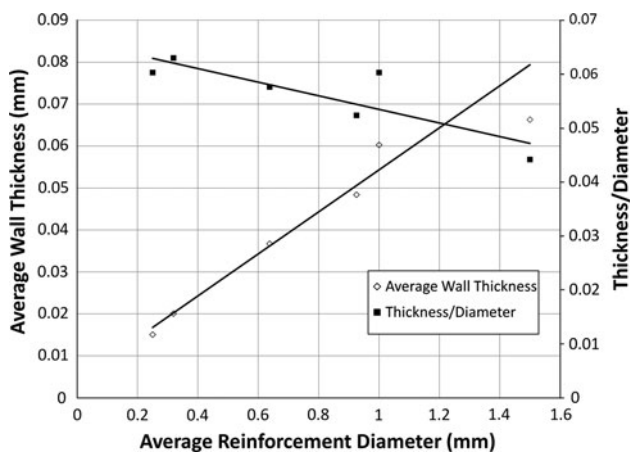


**Fig. 5** Dependence of average wall thickness and  $t/D$  ratio on reinforcement diameter

geometry and the average density of the sphere,  $\rho_{\text{sphere}}$ , as shown in Eq. (1) where  $\rho_{\text{Al}_2\text{O}_3}$  is the density of  $\text{Al}_2\text{O}_3$  and  $d$  is the internal diameter of the hollow sphere.

$$\rho_{\text{sphere}} = \rho_{\text{Al}_2\text{O}_3} \frac{\left(\frac{4}{3}\right)\pi\frac{D^3}{8} - \left(\frac{4}{3}\right)\pi\frac{d^3}{8}}{\left(\frac{4}{3}\right)\pi\frac{D^3}{8}} = \rho_{\text{Al}_2\text{O}_3} \left(1 - \frac{d^3}{D^3}\right) \quad (1)$$

The  $t/D$  ratio of the hollow spheres may be derived from the densities of  $\text{Al}_2\text{O}_3$  and hollow spheres by Eq. (2).

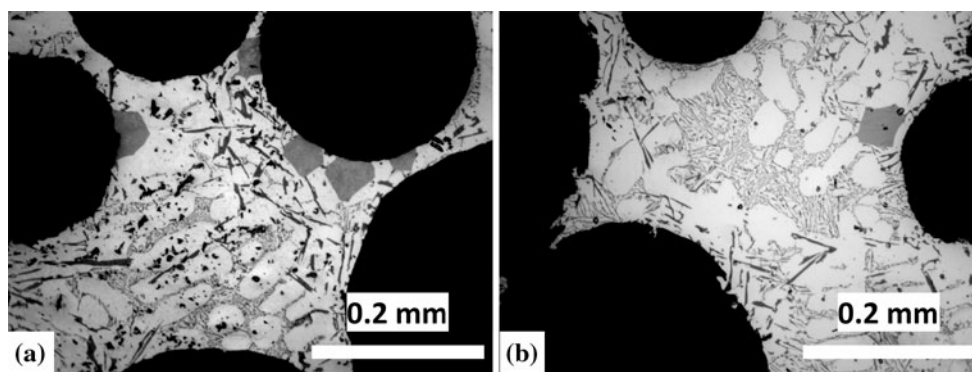
$$\frac{t}{D} = \frac{1}{2} \left[ 1 - \left( 1 - \frac{\rho_{\text{sphere}}}{\rho_{\text{Al}_2\text{O}_3}} \right)^{\frac{1}{3}} \right] \quad (2)$$

Figure 5 shows that though the average hollow sphere wall thickness increases with increasing sphere diameter, the  $t/D$  ratio decreases.

Table 2 presents the densities of the syntactic foam specimens along with the result of image analysis to determine the area percentage of matrix in the foam. Samples with loose particle size ranges (0–0.5, 1–2, and 0–2 mm of Fig. 4d–f) exhibit roughly the same  $A\%_{\text{matrix}}$ , with a lower limit of approximately 42 %, while the tight

hollow sphere size ranges (0.212–0.425, 0.425–0.85, and 0.85–1 mm of Fig. 4a, b, and c) all have a lower limit of  $A\%_{\text{matrix}}$  near 36–38 %. Though the hollow spheres were generally only encapsulated by the matrix, a portion of the spheres was broken and their interiors were also infiltrated at this pressure. The number fraction of infiltrated spheres, as determined by counting the number of filled versus hollow spheres on polished cylindrical sections with surface area  $160 \text{ mm}^2$ , is shown in Table 2. It can be seen that as the sphere size increases above 1 mm there is a significant increase in the number of filled spheres. This is likely due to the presence of more numerous critical size defects at higher hollow sphere diameters.

Figure 6 shows the microstructures of two composites having different preform densities. It is evident through comparison with Fig. 3 that the features of the matrix microstructure are refined by the presence of the hollow spheres. This is expected; as in addition to the influence of reactions between the matrix alloy and the reinforcement, the reinforcement can create a thermal and physical barrier to the solidification front that often results in the refinement of the microstructure near the reinforcement [34]. The interstices (i.e., the spaces between the hollow spheres occupied by the matrix alloy) varied in size due to the packing efficiency of the spheres, and showed indications that suggest that solidification began between the hollow spheres, and progressed to the surface of the spheres. Primary aluminum dendrites are visible between spheres in Fig. 6, along with eutectic phases in regions between dendrite arms that EDS analysis revealed to contain Cu, Al, Si, and O. Also, needle-like phases are visible that are typical of Al–Mn–Fe phases and  $\text{Al}_3\text{FeSi}$  and the presence of Al, Mn, Fe, and Si was confirmed via EDS. Finally, a blocky Si containing phase similar to that observed by Orbulov et al. [18] appears to nucleate on the surfaces of the hollow spheres, as evidenced by the several blocky clusters shown in Fig. 6a that in some cases appear to detach from the surface of the spheres as in Fig. 6b. In



**Fig. 6** Microstructure of A380– $\text{Al}_2\text{O}_3$  syntactic foams at  $\times 200$  containing hollow spheres ranging in size from **a** 0–0.5 mm and **b** 0.212–0.425 mm

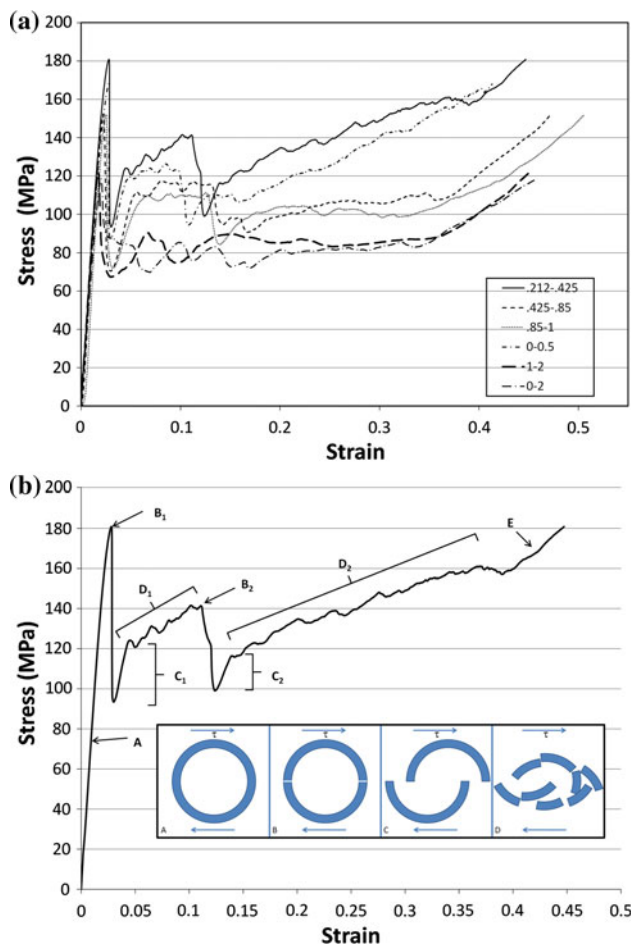


**Fig. 7** **a** Typical compressive stress–strain curves for A380–Al<sub>2</sub>O<sub>3</sub> syntactic foams and **b** a sample curve showing distinct deformation events. The *inset* shows the stages in fracture of hollow spheres along planes corresponding to the critical resolved shear stress

cases where the melt infiltrates the spheres, this phase nucleates on the irregular interior surfaces. The solidification microstructure within the infiltrated regions of the hollow sphere preform thus appears to be influenced in these cases by the thermal energy stored in the Al<sub>2</sub>O<sub>3</sub> hollow spheres during cooling and the insulating nature of Al<sub>2</sub>O<sub>3</sub>.

**Table 3** Summary of quasi-static compression data for A380–Al<sub>2</sub>O<sub>3</sub> syntactic foams

Sphere size range (mm)	Peak stress (MPa)	Plateau stress (MPa)	Densification strain (%)	Energy absorption (J/cm <sup>3</sup> )
0.212–0.425	181.2 ± 11.1	138.1 ± 8.9	43 ± 3	57.7 ± 6.2
0.425–0.85	152.2 ± 3.0	108.9 ± 3.1	49 ± 2	51.8 ± 1.8
0.85–1	149.1 ± 7.8	104.9 ± 5.0	49 ± 3	50.6 ± 4.0
0–0.5	164.4 ± 7.5	124.9 ± 5.4	40 ± 2	48.4 ± 2.4
1–2	120.4 ± 6.1	87.1 ± 8.8	47 ± 7	39.4 ± 4.0
0–2	122.7 ± 6.9	90.1 ± 6.0	45 ± 3	39.7 ± 3.1

All the data are reported as average ± standard deviation

### Mechanical properties

#### Quasi-static compression and energy absorption

Representative quasi-static engineering stress–strain curves are shown in Fig. 7a for each size range, and the average and standard deviation of peak strength, plateau strength, densification strain, and energy absorption are reported in Table 3.

During quasi-static compression, the A380–Al<sub>2</sub>O<sub>3</sub> syntactic foams exhibited a sharp primary drop and slightly more rounded secondary drop in the stress–strain curves which were the result of two near –45° shear bands of collapsed spheres that formed in the specimens coinciding with the plane of maximum shear (critical resolved shear stress). The fracture of the hollow spheres is, therefore, initiated by shear and is most likely to occur along the equatorial plane of the spheres as the wall thickness is smallest along this plane. Since this equatorial plane must support the entire shear force, it would be expected that the effective shear stress,  $\tau_{\text{eff}}$ , on this surface is greater than the applied shear stress,  $\tau_{\text{applied}}$  as shown in Eq. (3).

$$\tau_{\text{eff}} = \tau_{\text{applied}} \left[ \frac{\pi D^2}{4} / \frac{\pi(D^2 - d^2)}{4} \right] = \tau_{\text{applied}} / 4 \left( \frac{t}{D} - \frac{t^2}{D^2} \right) \cong \tau_{\text{applied}} / 4 \left( \frac{t}{D} \right) \tag{3}$$

Figure 7b shows a typical compressive stress–strain curve for an A380–Al<sub>2</sub>O<sub>3</sub> hollow sphere syntactic foam where distinct deformation events can be identified. The sequence of deformation events, labeled A–E in Fig. 7b from initial elastic strain to complete densification, can be linked to five stages of the deformation of the hollow spheres and surrounding matrix as shown schematically in Fig. 7b. These stages, shown in the inset of Fig. 7b, are summarized as follows:

- A. The foam undergoes elastic strain and the hollow spheres remain intact and undamaged.
- B. The critical resolved shear stress (CRSS) causes the spheres aligned with the weakest plane of the sample

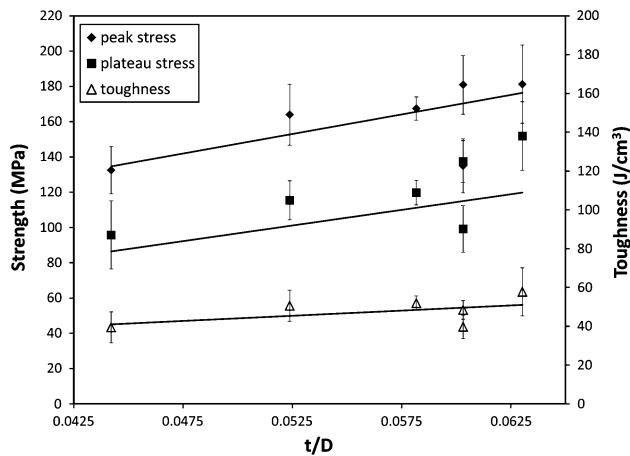


**Fig. 8** Average peak strength (filled diamonds), plateau strength (filled squares), and toughness (open triangles) versus  $t/D$  ratio. Error bars represent two standard deviations. All properties shown increase with increasing  $t/D$  ratio

(oriented at  $45^\circ$  angles to the applied compressive stress) to crack along their equatorial plane to form hemispheres, resulting in a sharp drop in the stress after a peak.

- C. The hemispheres slide past each other at a reduced stress corresponding to the matrix shear strength with some work hardening of the matrix.
- D. At sufficient stress, the hemispheres crush with simultaneous work hardening of the matrix until new shear bands form at the next weakest planes and steps B through D are repeated again.
- E. Work hardening produces enough stress that thereafter sphere crushing and collapse result in densification throughout the material.

It is evident in Fig. 7 that these stages become more pronounced as the average hollow sphere size and size range become smaller, which is likely due to packing efficiency,  $t/D$  ratio, and sphere quality. Since  $t/D$  decreases with increasing sphere diameter, it would be expected that larger spheres are subjected to higher effective shear strains and, therefore, foams utilizing larger spheres would show lower strength and toughness. Figure 8 summarizes the effect of sphere dimensions on the peak strength, plateau strength, and the toughness of A380–Al<sub>2</sub>O<sub>3</sub> syntactic foams. As the  $t/D$  ratio increases the peak strength, plateau strength and the toughness increase.

Figure 9 shows the specific energy absorption as a function of the area percentage of the A380 matrix determined by image analysis. The area percentage of A380 in the microstructure increases when hollow spheres are infiltrated or when the packing efficiency of the spheres is below optimum. The lowest area percentage of the matrix phase measured was 35.7 % for a foam containing 0.212–0.425 mm diameter

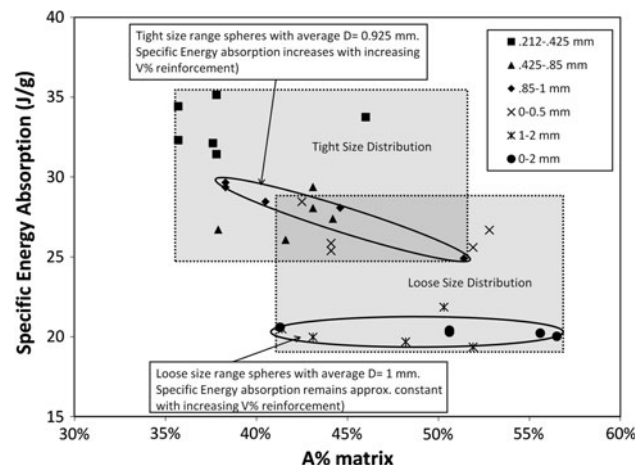


**Fig. 9** Plot of specific energy absorption versus area percentage of matrix. Tight size distributions result in higher overall reinforcement area percentage and higher specific energy absorption

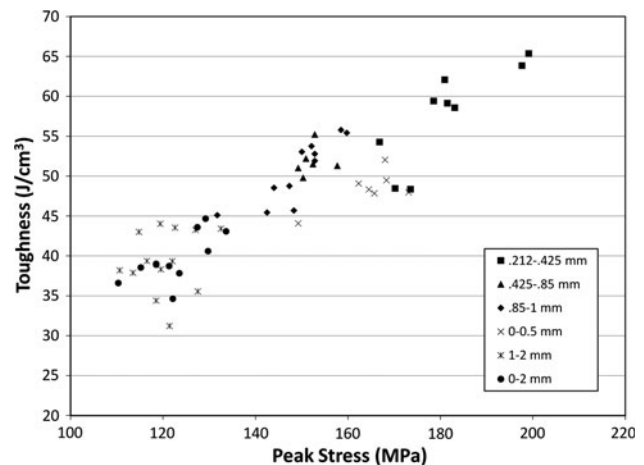


**Fig. 10** Plot of toughness versus peak stress for all reinforcement sizes. Reduced particle sizes result in increased toughness and peak stress

hollow spheres. The two rectangular shaded regions indicated in Fig. 9 correspond to foams containing tight size range and loose size range hollow spheres, respectively. The specific energy absorption of the foams tends to increase with decreasing sphere size, size distribution, and area percentage of matrix (packing efficiency of the hollow spheres). For the foams containing the tightest size distribution of hollow spheres (0.85–1 mm), the specific energy absorption increases with increasing area percentage of hollow spheres. This effect is not observed for looser size distributions, which is likely due to larger variability in sphere size, wall thickness, and porosity.

Figure 10 shows the relationship of peak stress to toughness for the various sizes of reinforcing hollow spheres. As expected from the previous discussion, the



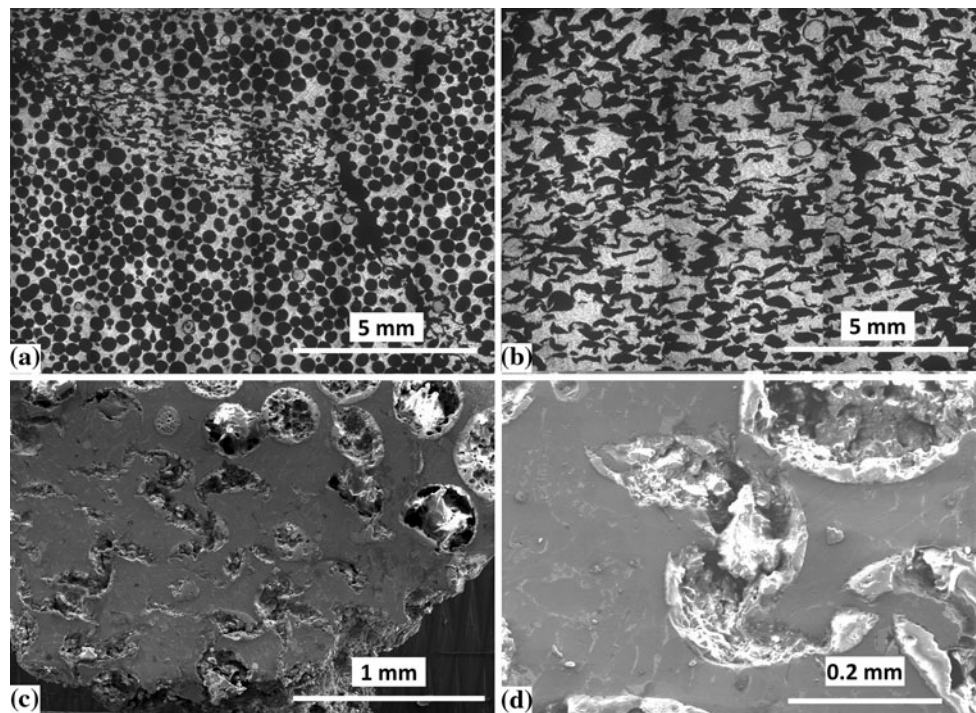


**Fig. 11** **a** Optical micrograph of cross section taken from sample tested to plateau stress region (*region D2* of Fig. 7b), **b** after sample was compressed until full densification (after *region E* of Fig. 7b),

**c** SEM micrograph of cross section of fractured specimen, **d** higher magnification SEM micrograph of deformation of hollow sphere at plane of maximum shear

toughness increases with measured peak stress, and smaller hollow sphere sizes perform significantly better than larger hollow sphere sizes due to their higher  $t/D$  ratio and tighter, more uniform size distribution.

Following compression testing, samples were sectioned and polished to reveal the cross section of the fractured composite for microscopy. Figure 11 shows sections taken through the center of the specimen in a direction aligned with the axis of the applied load (compressive load was applied at the top of the images). In Fig. 11a, c, and d, both hollow and infiltrated spheres can clearly be distinguished, as well as deformed (ellipsoidal) pores. Shear bands of fully collapsed pores are visible, and in the case of Fig. 11b, where the specimen was strained to 60 %, all spheres have been deformed to an ellipsoidal shape. Figure 11d shows a hollow sphere that has been deformed into two hemispheres and sheared along a 45° plane similar to the morphology expected from the schematic shown in the inset of Fig. 7b.

#### *Dynamic compression and strain rate sensitivity*

Syntactic foams containing 0.425–0.85 and 0.85–1 mm OD hollow spheres were tested using a Split Hopkinson bar apparatus to determine their high strain rate compressive characteristics. The general trend of the stress–strain graphs show a linear elastic region reaching a peak stress

followed by a plateau region at a stress drop on the order of 20–50 % of the initial peak stress due to the initiation of damage in the specimens. The shape of the quasi-static and high strain rate compressive stress–strain graphs is similar.

Figure 12 shows the peak stress and plateau stress over a range of strain rates from quasi-static to dynamic showing that despite the large variation in properties at high strain rates, the plateau strength and peak strength are essentially constant over the range of strain rates. To further identify strain rate sensitivity in the composites tested, a sensitivity parameter  $\Sigma$  is defined as [42]:

$$\Sigma = \frac{\sigma_d - \sigma_q}{\sigma^*} \frac{1}{\ln(\dot{\epsilon}_d / \dot{\epsilon}_q)} \quad (4)$$

where  $\sigma$  is the stress at a given strain,  $\sigma^*$  is the stress at a given strain at a reference strain rate of  $10^{-3} \text{ s}^{-1}$ ,  $\dot{\epsilon}$  is the strain rate, and the subscripts  $d$  and  $q$  refer to dynamic and quasi-static testing, respectively. The peak stress was used for the dynamic, quasi-static, and reference stresses after the analysis of Balch et al. [8] due to the unique deformation behavior of metal foams in comparison to alloys or composites and  $\Sigma$  is plotted versus strain rate in Fig. 12b. The average calculated sensitivity parameter falls below 0.01, which is expected for similar aluminum alloys [42] leading to the conclusion that the strain rate sensitivity in the case of the A380–Al<sub>2</sub>O<sub>3</sub> syntactic foams is primarily dependent on the matrix properties and not greatly affected

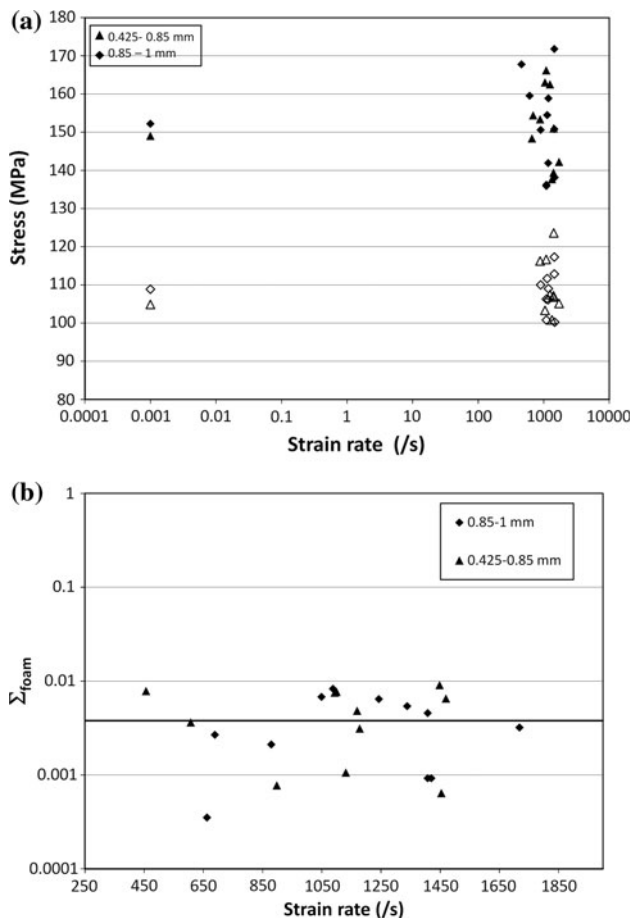


**Fig. 12** **a** Peak stress (*solid marker*) and plateau stress (*open marker*) versus strain rate showing no significant strain rate dependence of either property. **b** Strain rate sensitivity parameter  $\Sigma$  versus strain rate showing no strain rate dependence of peak stress in dynamic strain rate regime

by the presence of the  $\text{Al}_2\text{O}_3$  hollow spheres within the range investigated in this study.

Comparison of quasi-static and dynamic properties of metallic foams for energy absorption

Metal foams and MMSFs have been proposed for energy absorption applications such as automotive bumpers, personal protective gear, and blast armor. The design of such structures depends on the amount of energy the material can absorb per unit mass (specific energy absorption in J/g) and the stress at which this energy is absorbed (the plateau strength), and generally includes a buffer plate that is sufficiently stiff to transfer the energy of the blast to the energy absorbing material behind it. In order for the energy absorbing material to be effective, the peak and plateau strengths must be predictable and uniform, and the specific energy absorption must be large at that plateau strength (this governs the required thickness of the material). The

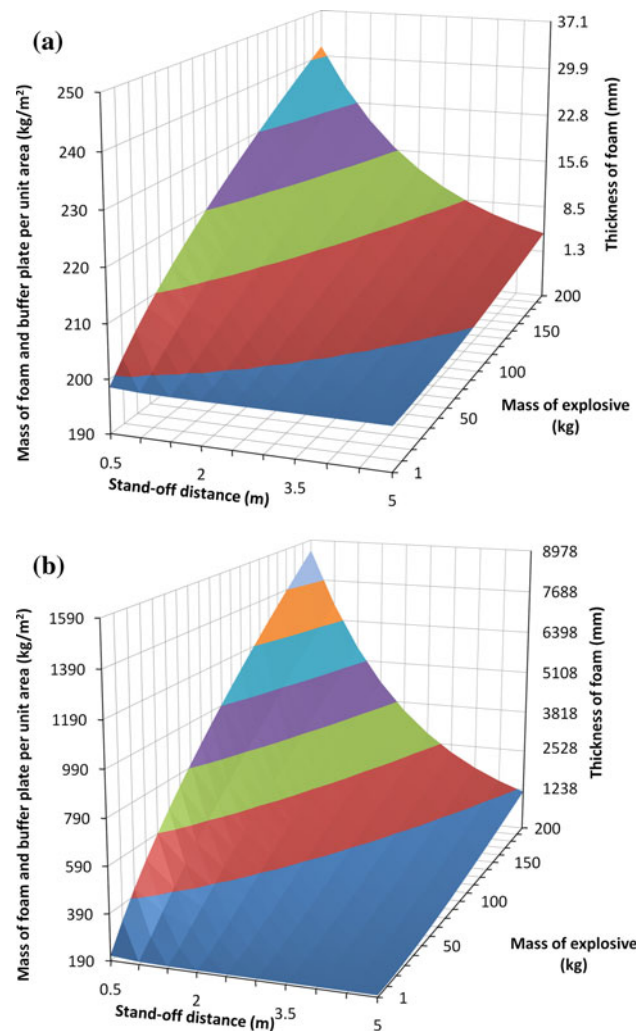


**Fig. 13** Calculated blast amelioration maps for TNT exploding in air against a 1-inch-thick steel buffer plate coupled with **a** an aluminum syntactic foam **b** a CYMAT metal foam

material is then chosen where the force transmitted to the substructure at the plateau stress is below a critical level that would result in structural damage. The impulse ( $I$ ) that the explosion of a given mass ( $M$ ) of trinitrotoluene (TNT) that a structure will need to absorb at a given distance ( $x$ ) in air may be determined by the following empirical equation (5) [1]:

$$I \approx B_1 M^{1/3} e^{-C^* \left( x/M^{1/3} \right)} \quad (5)$$

where  $B_1 = 5000 \text{ sPa}(\text{kg})^{-1/3}$  and  $C^* = 1.3 (\text{kg}^{1/3})/\text{m}$ . This impulse imparts a momentum to a unit area of a buffer plate, accelerating it to a given velocity. The kinetic energy of the buffer plate must then be dissipated by the foam material before it reaches the structure. The thickness of the foam material ( $t_{\text{foam}}$ ) required to dissipate the kinetic energy created by the impulse of the explosion against a

buffer plate of thickness  $d_b$  and having density  $\rho_b$  is given by.

$$t_{\text{foam}} = \frac{I^2}{2\rho_b d_b U} \quad (6)$$

and the total mass per unit area ( $m_T$ ) of the foam and buffer plate may be calculated by [2]

$$m_T = \rho_b d_b + \frac{I^2}{2\rho_b d_b U_p} \quad (7)$$

where  $U$  and  $U_p$  are the volumetric and specific energy absorption of the foam, respectively.

The blast amelioration map for a syntactic foam having a plateau strength of 90 MPa, a volumetric energy absorption of 55000 kJ/m<sup>3</sup>, and specific energy absorption of 39.29 J/g and a 25.4-mm steel buffer plate is shown in Fig. 13a. A similar map drawn from data presented in [1] for CYMAT aluminum foam having a plateau strength of 1 MPa, a volumetric energy absorption of 200 kJ/m<sup>3</sup>, and specific energy absorption of 1.29 J/g and a 25.4-mm steel buffer plate is shown in Fig. 13b. It can be seen that the aluminum syntactic foam can absorb more energy by crushing than the CYMAT foam, as the thickness and resulting weight of the syntactic foam system is far less than that of the CYMAT foam. For example, to absorb the energy of a blast from 100 kg of TNT at a stand-off distance of 2 m, 1 m<sup>2</sup> of CYMAT foam would need to be 2216 mm thick and together with the buffer plate would weigh 542 kg. A square meter of the aluminum syntactic foam would need to be merely 8.1 mm thick and together with the buffer plate would weigh only 209 kg. This example demonstrates the advantage of using MMSFs in systems for blast protection owing to their superior specific energy absorption in comparison to open-celled foams.

## Conclusions

The microstructure and quasi-static and dynamic mechanical properties of A380–Al<sub>2</sub>O<sub>3</sub> hollow sphere syntactic foams have been determined for foams with six different microsphere sizes and different size ranges. The quasi-static compressive stress–strain curves exhibit distinct deformation events corresponding to initial failure of the foam at the critical resolved shear stress and subsequent failures and densification events until the foam is deformed to full density. The peak strength, plateau strength, and toughness of the A380–Al<sub>2</sub>O<sub>3</sub> syntactic foams synthesized in the present study increase with increasing  $t/D$  ratio. Since  $t/D$  was found to increase with decreasing sphere diameter, the foams produced with finer hollow spheres result in improved performance. Tight size ranges generally outperformed looser size ranges at equivalent area percentages, and in the case of

the tightest size distribution, the specific energy absorption increased with increasing area percentage of spheres. Split Hopkinson bar tests of syntactic foams conducted at strain rates between 880 and 1720 s<sup>-1</sup> showed that the properties of syntactic foams containing 0.425–0.85 to 0.85–1 mm diameter hollow spheres are not strain rate-dependent and, therefore, under blast conditions, performance would be similar to that determined from quasi-static tests.

**Acknowledgements** This research was supported by the U.S. Army-TARDEC through TACOM R&D Contract# W56HZV-08-C-0716. The authors would also like to acknowledge and thank C-E Minerals for providing the ALODUR alumina hollow sphere material. Disclaimer: Reference herein to any specific commercial company, product, process, or service by trade name, trademark, manufacturer, or otherwise, does not necessarily constitute or imply its endorsement, recommendation, or favoring by the United States Government or the Department of the Army (DoA). The opinions of the authors expressed herein do not necessarily state or reflect those of the United States Government or the DoA, and shall not be used for advertising or product endorsement purposes.

## References

1. Evans AG, Hutchinson JW, Ashby MF (1999) Prog Mater Sci 43:171
2. Ashby MF, Evans AG, Hutchinson JW (1998) Cellular metals, a design guide. Cambridge University, Engineering Department, Cambridge
3. Chino Y, Dunand DC (2008) Acta Mater 56:105
4. Feng Y, Tao N, Zhu Z, Hu S, Pan Y (2003) Mater Lett 57:4058
5. Kanahashi H, Mukai T, Yamada Y, Shimojima K, Mabuchi M, Aizawa T, Higashi K (2001) Mater Sci Eng A 308:283
6. Yamada Y, Shimojima K, Sakaguchi Y, Mabuchi M, Nakamura M, Asahina T, Mukai T, Kanahashi H, Higashi K (1999) J Mater Sci Lett 18:1477
7. Rohatgi PK, Kim JK, Gupta N, Alaraj S, Daoud A (2006) Compos A 37:430
8. Balch DK, O'Dwyer JG, Davis GR, Cady CM, Gray GT III, Dunand DC (2004) Mater Sci Eng A 391:408
9. Balch DK, Dunand DC (2006) Acta Mater 54:1501
10. Dou ZY, Jiang LT, Wu GH, Zhang Q, Xiu ZY, Chen GQ (2007) Scr Mater 57:945
11. Wu GH, Dou ZY, Sun DL, Jiang LT, Ding BS, He BF (2007) Scr Mater 56:221
12. Zhang Q, Lee PD, Singh R, Wu G, Lindley TC (2009) Acta Mater 57:3003
13. Tao XF, Zhang LP, Zhao YY (2009) Mater Des 30:2732
14. Tao XF, Zhao YY (2009) Scr Mater 61:461
15. Zhao Y, Tao X, Xue X (2008) Manufacture and mechanical properties of metal matrix syntactic foams. In: Processing, Properties and Performance of Composite Materials, Materials Science and Technology, Pittsburgh, pp 2607
16. Zhang LP, Zhao YY (2007) J Compos Mater 41:2105
17. Orbulov IN, Dobránszky J (2008) Producing metal matrix syntactic foams by pressure infiltration. Period Polytech, Mech Eng 52:35
18. Orbulov IN, Dobránszky J, Nemeth A (2009) J Mater Sci 44:4013. doi:10.1007/s10853-009-3552-2
19. Orbulov IN (2012) Mater Sci Eng A 555:52
20. Orbulov IN, Ginsztler J (2012) Compos A 43:553
21. Orbulov IN (2013) Mater Sci Eng A 583:11

22. Orbulov IN, Májlinger K (2013) *Mater Des* 49:1
23. Kiser M, He MY, Zok FW (1999) *Acta Mater* 47:2685
24. Drury WJ, Rickles SA, Sanders TH Jr, Cochran JK (1989) In: Lee EW, Chia EH, Kim NJ (eds) *Light-weight alloys for aerospace applications*. The Minerals Metals and Materials Society, Warrendale, p 311
25. Santa Maria JA, Schultz BF, Ferguson JB, Rohatgi PK (2013) *Mater Sci Eng A* 582:415
26. Palmer RA, Gao K, Doan TM, Green L, Cavallaro G (2007) *Mater Sci Eng A* 464:85
27. Rabiei A, Vendra LJ (2009) *Mater Lett* 63:533
28. DeFouw JD, Rohatgi PK (2011) Low density magnesium matrix syntactic foams. In *Supplemental Proceedings: Volume 2: Materials Fabrication, Properties, Characterization, and Modeling*, The Minerals, Metals and Materials Society, Warrendale, p 797
29. Rocha Rivero GA, Schultz BF, Ferguson JB, Gupta N, Rohatgi PK (2013) *J Mater Res* 28:2426. doi:[10.1557/jmr.2013.176](https://doi.org/10.1557/jmr.2013.176)
30. Daoud A (2008) *Mater Sci Eng A* 488:281
31. Neville BP, Rabiei A (2008) *Mater Des* 29:388
32. Castro G, Nutt SR (2012) *Mater Sci Eng A* 535:274
33. Mondal DP, Majumder JD, Jha N, Badkul A, Das S, Patel A, Gupta G (2012) *Mater Des* 34:82
34. Mortensen A, Jin I (1992) *Int Mater Rev* 37:101
35. Gupta N, Shunmugasamy VC (2011) *Mater Sci Eng A* 528:7596
36. Gupta N, Luong DD, Rohatgi PK (2011) *J Appl Phys* 109:1
37. Kapoor R, Nemat-Nasser S (1998) *Mech Mater* 27:1
38. Puchi ES, Staia MH, Villalobos C (1997) *Int J Plasticity* 13:723
39. Bäckerud L, Chai G, Tamminen J (1990) *Solidification characteristics of aluminum alloys volume 2 foundry alloys*. AFS/Skanaluminium, Des Plaines
40. Gowri S, Samuel FH (1994) *Metall Mater Trans A* 25:437
41. Samuel AM, Samuel FH (1995) *J Mater Sci* 30:1698. doi:[10.1007/BF00351598](https://doi.org/10.1007/BF00351598)
42. San Marchi C, Cao F, Kouzeli M, Mortensen A (2002) *Mater Sci Eng A* 337:202